Enhanced α-Mn$_2$O$_3$ nanorods synthesized by one-pot hydrothermal route for supercapacitors

B. Arjun Kumar[1], G. Ramalingam[1,*], Baskaran Rangasamy[2,*], Abhishek Lahiri[3], H. H. Somaily[4,5], Jamila S. Alzahrani[6], and M. S. Al-Buriahi[7,*] (iD)

[1] Quantum Materials Research Lab (QMRL), Department of Nanoscience and Technology, Alagappa University, Karaikudi, Tamil Nadu 630003, India

[2] Energy Storage Materials & Devices Lab, Department of Physics, School of Mathematics and Natural Sciences, The Copperbelt University, Riverside, PO Box 21692, Kitwe, Zambia

[3] Department of Chemical Engineering, Brunel University-London, Uxbridge UB83PH, UK

[4] Research Center for Advanced Materials Science (RCAMS), King Khalid University, P.O. Box 9004, Abha 61413, Saudi Arabia

[5] Department of Physics, Faculty of Science, King Khalid University, P.O. Box 9004, Abha, Saudi Arabia

[6] Department of Physics, College of Science, Princess Nourah bint Abdulrahman University, P.O. Box 84428, Riyadh 11671, Saudi Arabia

[7] Department of Physics, Sakarya University, Sakarya, Turkey

ABSTRACT

Pseudo-capacitors are the emerging energy storage devices which forms a bridge between batteries and conventional capacitors. In the present work, α-Mn$_2$O$_3$ nanorods have been synthesized by one-pot acid-assisted hydrothermal method for supercapacitor applications. The α-Mn$_2$O$_3$ nanorod electrode is characterized by X-ray diffraction, SAED, Transmission Electron Microscopy (TEM), EDX and tested for supercapacitor application. XRD results indicate polycrystalline nature of α-Mn$_2$O$_3$. TEM results reveal an optimum nanorod diameter of 7 nm and length of 100 nm with high aspect ratio of 1:4. The high aspect ratio obtained by acid assisted one-pot hydrothermal route and the possible growth mechanism are explored. The structural and morphological investigations reveal that the acid implementation and suitable reaction temperature plays a crucial factor in the formation of homogeneous α-Mn$_2$O$_3$ nanorods. The cyclic voltammetry redox kinetics indicates pseudo-capacitive behavior with an excellent specific capacitance of 1377 F g^{-1} at 5 mVs^{-1}. The galvanostatic charge–discharge investigations reveal an excellent 69% capacitance retention even after 1000 cycles. Ex-situ SEM, XRD and impedance spectroscopy investigations have been carried out to understand the nature of α-Mn$_2$O$_3$ nanorod after 1000 cycles. The synergetic effect of nanorod architecture, nanoparticle presence has been discussed in terms of excellent supercapacitive behavior.

Address correspondence to E-mail: ramanloyola@gmail.com; baskaran.rangasamy@cbu.ac.zm; mohammed.al-buriahi@ogr.sakarya.edu.tr

⚊ Springer

1 Introduction

Supercapacitors play a major role as energy storage device in electronic devices, electric vehicles, industries and even to run huge cranes. Especially pseudo-capacitors store electric energy on the surface of electrodes by rapid redox reactions. Pseudo-capacitors exhibit higher capacitance and energy density than electric double layer capacitors (EDLC) and also higher power densities while compared to batteries [1]. However, the energy density of pseudo-capacitors is much lower than batteries. Also, the pseudo-capacitors deliver inferior cycle life and rate capability than EDLC. In order to overcome poor energy density and cycling stability issues, research efforts by synthesizing electrode materials with novel architectures have been targeted [2]. Among various materials, manganese oxides are promising electrodes which are applicable in various energy devices especially in batteries and supercapacitors. Manganese oxides exist in various forms such as MnO_2, Mn_2O_3 and Mn_3O_4 all of which have shown good efficiency in energy storage devices [1–3]. Manganese (MnO_2) oxide is a good choice of pseudo-capacitor material among all the transition metals. This is because of MnO_2 has a high-specific capacitance 10^{18} mAh g^{-1} (theoretical), natural abundance, excellent structural flexibility and low cost [4].

In the past decade, various types of Mn_2O_3 nanostructure morphologies such as nanorods, hollow sphere, nanosheets, polyhedral, mesoporous structures have been synthesized by various techniques [5–9]. Zhen-Yu Li et al. [10] developed Mn_2O_3 nanowalls through hydrothermal technique which delivered an excellent capacitance of 480 Fg^{-1} at 10 mVs^{-1} in 6 M KOH electrolyte. In a similar manner, W. Li et al. synthesized a porous Mn_2O_3 nanocubes by hydrothermal method and used as electrode material which delivered specific capacitance of 191 Fg^{-1} and high-rate capability [11]. Changzhou Yuan et al. [12] developed a flower like MnO_2 with 2D-mesoporous nanosheet by co-precipitate method through acid medium that exhibited specific capacitance of 298 Fg^{-1} at a current density of 0.117 Ag^{-1}. In another report, hydrothermally grown branched α-MnO_2 nanorod electrode delivered specific capacitance, at the current density of 2 Ag^{-1}, of 182 Fg^{-1} which was developed by Xiaohui Su et al. [13]. Many researchers reported different phases of manganese oxides with various nano architectures synthesized by hydrothermal and other chemical routes which indicate a relatively high specific capacitance values. However, depends upon the dimension and shape of the nano materials, variations in electrochemical performances are observed which reveals a careful synthesis approach is essential to achieve an excellent specific capacitance and cyclability [5–13]. In particular, features of nanomaterials are mainly based on their size, dimensionality, chemical composition, phase structure which are mainly depending on synthesis method. In this scenario, a novel strategy is required to synthesize Mn_2O_3 nano architectures for energy storage and conversion device uses.

In the current study, a new low temperature acid assisted one-pot hydrothermal method has been used to synthesize homogeneous and high aspect ratio α-Mn_2O_3 nanorods. Structure and morphology investigations have been carried out on α-Mn_2O_3 nanorod electrodes by using XRD, SAED and TEM analyses. A pseudo-capacitor has been constructed with a free standing α-Mn_2O_3 nanorod coated on nickel foam. The enhancement of specific capacitance of pseudo-capacitor with α-Mn_2O_3 electrode has been analyzed in terms of aspect ratio, dimension and redox kinetics of nanorods.

2 Experimental work

2.1 Materials

The needed chemicals such as Hydrochloric acid (HCl), Sulfuric acid (H_2SO_4) and Potassium permanganate ($KMnO_4$) (Merck AR grade) have been used for the synthesis of Mn_2O_3 nanorods. De-ionized (DI) water is collected from double distillation setup system which is used for the acid assisted hydrothermal synthesis.

2.2 Synthesis of Mn_2O_3 nanorods

The synthesis of Mn_2O_3 nanorods has been carried out by one-pot hydrothermal method. An equal quantity of nitric acid (HNO_3) and sulfuric acid (H_2SO_4) in 1:1 ratio are mixed homogeneously in a beaker. A 2 g of $KMnO_4$ is dissolved in de-ionized water and then the solution of $KMnO_4$ is added drop wise at a rate of 0.25 ml m^{-1}in with the acid solution using a burette with continuous stirring. The solution mixture is allowed for 12 h of stirring at 30 °C. The

reaction mixture is then transferred to a Teflon autoclave vessel and sealed. The steel container with the sample mixture is kept in an oven at 200 °C for 5 h. After cooling down, the resultant material/solution is then centrifuged at 8000 rpm for 10 min. The supernatant is decanted and the residuals are washed with HCl and DI water (in 1:3 ratio) for five times. The obtained Mn_2O_3 sample is dried for 24 h in a vacuum oven at 120 °C to remove moisture and water contents.

2.3 Construction of supercapacitor

In order to construct a supercapacitor, free standing Mn_2O_3 nanorod sample is coated on nickel foam in a step by step process as described below. Nickel foam, as a current collector, is used in the present work which is thoroughly cleaned by sonicating in 1 M HCl for 30 min and then washed repeatedly with deionized water before use. After cleaning, the nickel foam is dried overnight in a vacuum oven. The working electrodes are prepared by mixing carbon black, polyvinylidene fluoride (PVdF), and active material (Mn_2O_3 nanorods) in 5:15:80 weight ratios with anhydrous N-methyl-2-pyrrolidone (NMP) as a solvent. The resultant slurry is coated on the pre-cleaned nickel foam and dried at 80 °C in a vacuum oven for 12 h. A free standing Mn_2O_3 nanorods coated on nickel foam is obtained after drying which is used as symmetry electrodes for the construction of supercapacitor device. A beaker type supercapacitor is constructed with symmetry Mn_2O_3/Ni working electrodes and Ag/gCl as reference electrode immersed in 1 M aqueous KOH electrolyte in a clean room atmosphere.

2.4 Material characterizations

The as synthesized Mn_2O_3 nanorod is characterized by powder X ray diffraction measurements (PAN analytical XPERT-PRO X-ray diffractometer) with Cu Kα radiation (λ = 1.54056 Å) in the 2θ range of 5° to 80° at 1° min^{-1} scan rate. Fourier transform infrared spectroscopy is performed using Thermo Nicolet 380 FTIR spectrophotometer. The SAED pattern of the Mn_2O_3 sample and morphology of the Mn_2O_3 nanorod is observed by using transmission electron microscopy (JEOL/JEM 2100). High Resolution Scanning Electron Microscope, electron mapping and energy-dispersive spectrum are taken using FEI Quanta FEG 200. Particle size distribution is employed on TEM images using image J software. A Biologic SP-300 electrochemical workstation is used to investigate cyclic voltammetry, galvanostatic charge–discharge, and electrochemical impedance spectra.

3 Results and discussion

3.1 Physical and morphological analysis

Figure 1a–h shows the X-ray diffraction, electron diffraction pattern and TEM images of the as synthesized Mn_2O_3 nanorods. The X-ray diffraction pattern of Mn_2O_3 sample (Fig. 1a) indicates reflection peaks at 18.5°, 33.3°, 39.1°, 45.2°, 56.1° and 67.4° corresponding to the planes (200), (222), (400), (332), (440), and (622) respectively which reveals α-Mn_2O_3 formation. The indexed peaks of as synthesized Mn_2O_3 sample are consistent with JCPDS (41-1442) which indicates cubic phase formation with a space group of Ia-3(206) [14, 15]. The appearance of most of the peaks corresponding to different planes indicates polycrystalline nature of α-Mn_2O_3.

Figure 1b describes SAED pattern of α-Mn_2O_3 nanorods. The SAED pattern shows four concentric electron diffraction rings that confirms the presence of (200), (222), (400) and (622) planes which are in concurrence with XRD results. The increase in radius of the rings indicates decrease in d-spacing of these planes. Figure 1c–g shows the TEM-morphological features of as-synthesized α-Mn_2O_3 nanorods at different magnifications. The TEM image observed in Fig. 1c at 100 nm indicates the obtained α-Mn_2O_3 nanorods are homogeneously distributed. Figure 1d, e shows the α-Mn_2O_3 nanorods morphology at 50 and 20 nm magnifications reveals uniform shape and sizes of the nanorods. Figure 1f, g shows the TEM image of α-Mn_2O_3 at very high magnifications such as 10 and 5 nm which clearly indicating the width of nanorods in the range of 5–7 nm and the lengths in the range of 80–120 nm in the observed region. Figure 1h depicts the particle size distribution of nanorods determined from image J software which indicates the width of nano rods is in the range of 4 ~ 10 nm. The average width of the nanorods is about 7 nm and the length is about 100 nm which gives an aspect ratio of 14. The TEM morphology of α-Mn_2O_3 indicates formation of uniform nanorods
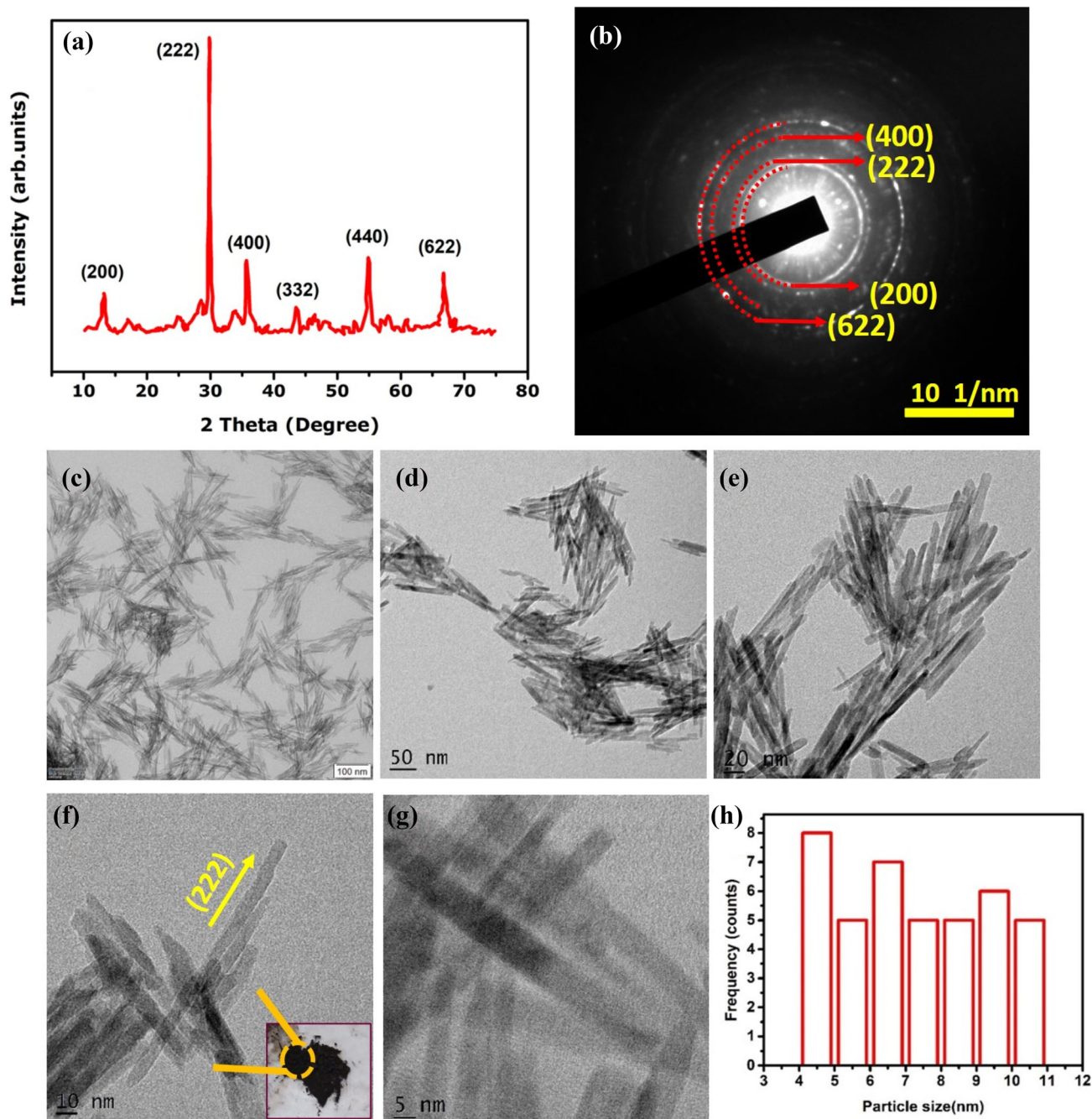
Fig. 1 a XRD pattern of α-Mn$_2$O$_3$ nanorods before and after redox cycling **b** SAED pattern; **c–g** TEM images in various magnifications and **h** particle size distribution of as synthesized of α-Mn$_2$O$_3$ nanorods

which is due to gradual addition of KMnO$_4$ with HCl:H$_2$SO$_4$ followed by hydrothermal treatment [14, 16, 17].

The growth of nanorod based on the hydrothermal synthesis approach is illustrated in Fig. 2. Since the presence of mild acid medium acts as a capping agent during hydrothermal synthesis of α-Mn$_2$O$_3$ nanorods, a uniform growth of nanorods with step-by step

development is expected. The growth of α-Mn$_2$O$_3$ nanorods consists of nucleation, grain development, and combination of grains in a particular direction due to the presence of ligands followed by the development of nanorods.

As discussed in XRD analysis, the poly crystalline α-Mn$_2$O$_3$ nanorods are mostly oriented along (222) plane through which the nano particles are perfectly

aligned to grow nanorods. However, there might also be grain growth along the other planes as observed in XRD and SAED results since the α-Mn$_2$O$_3$ has a polycrystalline nature [18]. This sort of nanorod growth lowers the general surface energy because of the disposal of energy related with unsatisfied bonds [19]. Abatement in length of the α-Mn$_2$O$_3$ nanorods during growth is carried out by restricted lengthwise collection of nanoparticles. The sharp tip of a few α-Mn$_2$O$_3$ nanorods emerges due to surface energy and surface dissemination occurred during the development of the nanostructures [20, 21].

3.2 EDX analysis of α-Mn$_2$O$_3$ nanorods

Figure 3a–c shows elemental mapping along with EDX spectrum of α-Mn$_2$O$_3$ nanorods. Figure 3a, b indicates presence of Mn and Oxygen in the selected region of the α-Mn$_2$O$_3$nanorod sample. The EDX spectrum (Fig. 3c) shows the presence of manganese and oxygen atom in the α-Mn$_2$O$_3$ nanorods without any impurities. The table indicates atomic and weight percentage of elements such as Mn, and Oxygen present in the α-Mn$_2$O$_3$ sample. The presence of carbon (C) indicates the usage of carbon grid in the EDX analysis. The stoichiometric weight percentage of Mn and O are found to be 56.9% and 36.6%, respectively. EDX analysis authenticates the presence of manganese and oxygen in the α-Mn$_2$O$_3$ compound.

3.3 FTIR analysis

Figure 4 shows FTIR spectrum of bare α-Mn$_2$O$_3$ nanorods. The significant peaks observed at 703, 585, 562 and 520 cm^{-1} are attributed to Mn–O bonds present in α-Mn$_2$O$_3$ nanorods. The peaks observed at 585 and 520 cm^{-1} are ascribed to stretching vibrations of Mn–O and O–Mn bonds [22, 23]. The shoulder bands observed at 684 and 608 cm^{-1} are ascribed to asymmetric and symmetric stretching vibrations of Mn–O–Mn bond in α-Mn$_2$O$_3$ [24, 25]. The vibration bands observed at 703, 585, 562, 520, and 490 cm^{-1} [24, 25] indicates the formation of manganese oxide. A slight hump observed at 1386 cm^{-1} is attributed to the finger print stretching vibration of carbonate group [24, 25] which might be due to the surface adsorption. A slight peak observed at 970 cm^{-1} and a strong peak at 1116 cm^{-1} might be due to OH hydroxyl bond connected to the Mn atom [23, 26]. A slight broad hump observed around 3450 and 2354 cm^{-1} are ascribed to the moisture and CO$_2$ absorption from the surrounding environment [27]. The broad peak observed at 3450 cm^{-1} and a sharp peak at 1623 cm^{-1} are attributed to stretching and bending vibrations of OH group of remaining water molecules resulted due to the surface adsorption of the α-Mn$_2$O$_3$ sample. However, nature of broad peaks indicates the absorption of moisture and CO$_2$ is not prominent in the sample.

3.4 Supercapacitor application

The electrochemical properties of α-Mn$_2$O$_3$ nanorods in 1 M aqueous KOH electrolyte have been analysed using cyclic voltammetry (CV), electrochemical impedance spectroscopy (EIS), and galvanostatic charge–discharge (GCD). Figure 5a depicts the cyclic voltammetry plot of α-Mn$_2$O$_3$ recorded between 0.0 and 0.5 V with the Ag/AgCl reference electrode at different scan rates. The specific capacitance (C_{sp}) is computed from the CV curves employing the established equation,
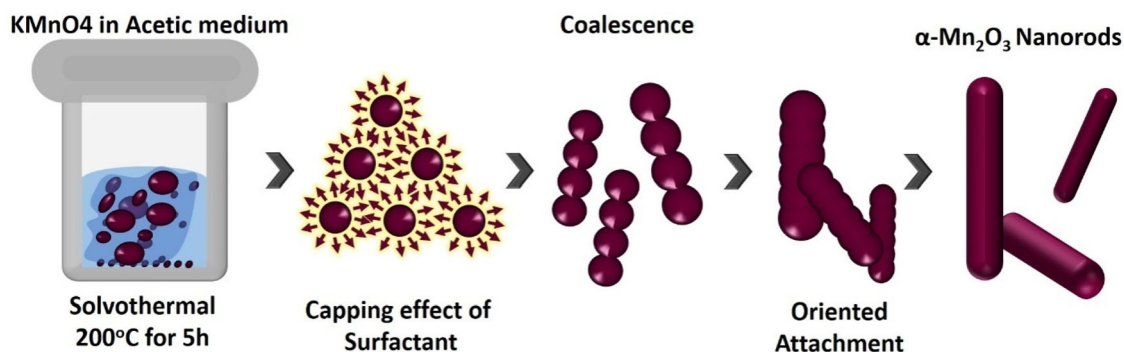

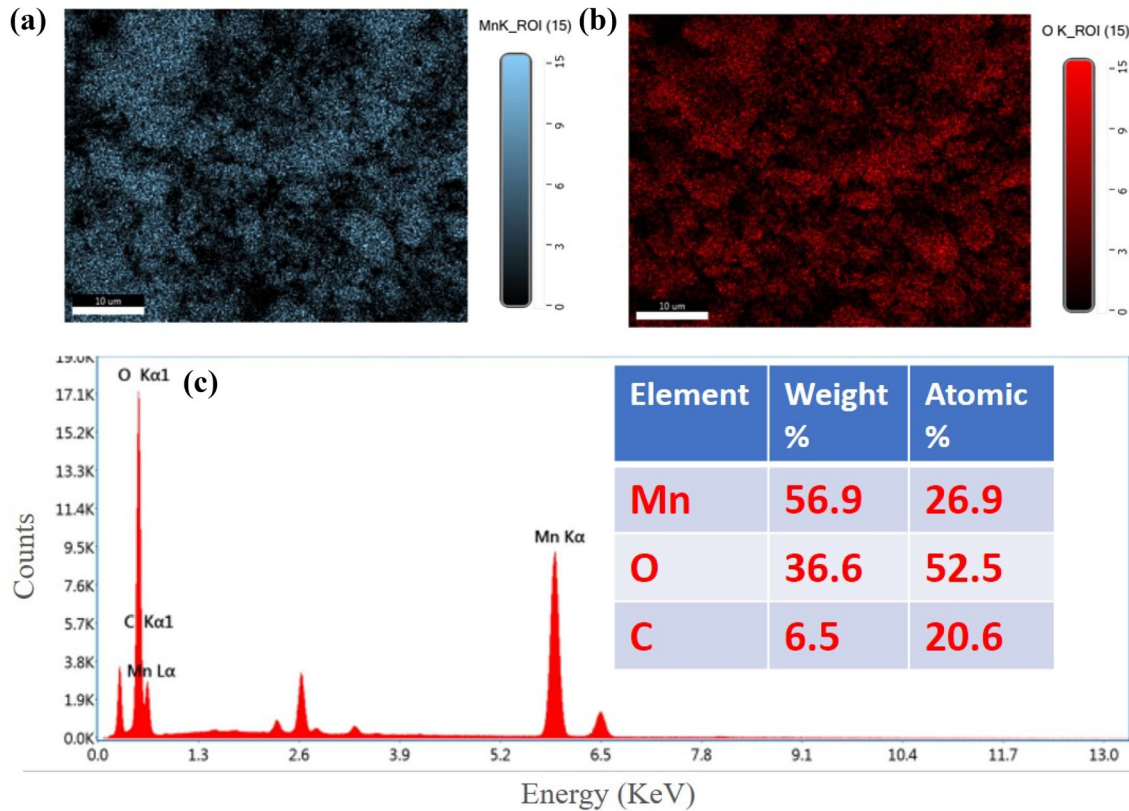Fig. 2 Schematic representation of the possible growth of α-Mn$_2$O$_3$ nanorods in a hydrothermal reactor

Fig. 3 **a**, **b** Elemental mapping of α-Mn$_2$O$_3$ nanorods; **c** EDX plot of α-Mn$_2$O$_3$ nanorods
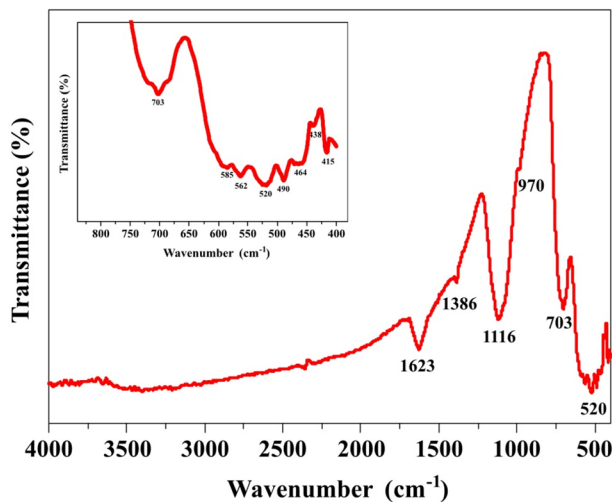

Fig. 4 FTIR spectrum of bare α-Mn$_2$O$_3$ nanorods (Inset: Zoomed FTIR spectrum in the 400–850 cm^{-1} region)

$$C_{sp} = \frac{1}{Vmv} \int i\,dV, \tag{1}$$

where i (A) is the applied current, V (V) is the maximum voltage, v is the scan rate and m (g) is the active mass of the electrode. We found that the obtained values of specific capacitance at various scan rates of 5, 10, 20, 30, 50, 80 and 100 mVs^{-1} are 1377, 1134, 915, 750, 516, 328 and 255 F g^{-1}. The CV curves show broad oxidation and reduction peaks which are attributed to Mn^{+3} to Mn^{+4} and Mn^{+4} to Mn^{+3}, respectively [28]. The hydroxyl and proton ions are mobile in the electrolyte which reacts with the α-Mn$_2$O$_3$ nanorod electrode during redox reactions that facilitates charge transfer reaction in the electrode. α-Mn$_2$O$_3$ nanorods delivers high specific capacitance of ~ 1377 F g^{-1} at 5 mVs^{-1} due to the uniform size and high aspect ratio of the nanorods which generates large active sites and rapid ion transport to the surface [10, 15]. The nanorod architecture has shortest diffusion path ways, minimized grain boundary resistance that enable fast redox reaction and excellent electrochemical performance of the electrode. Furthermore, all the CV curves possess clear redox peaks of α-Mn$_2$O$_3$ even at high scan rate of 100 mVs^{-1}. The appearance of clear redox peaks in the CV plot indicates pseudocapacitive nature of the supercapacitor.
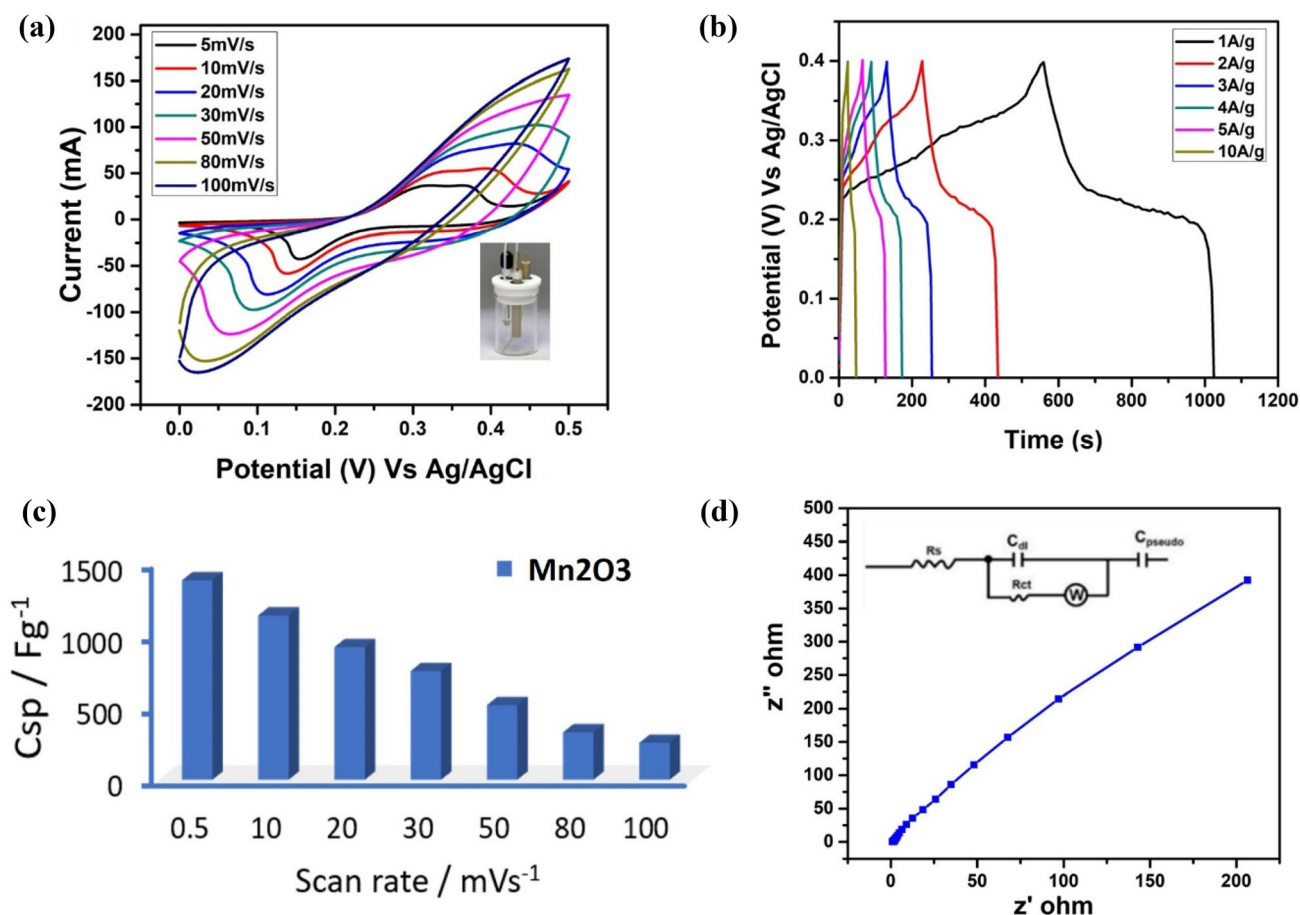
Fig. 5 a CV curves of α-Mn$_2$O$_3$ recorded within the potential range of 0.0–0.5 V at various scan rates. **b** GCD curves measured at various current densities in the potential range of 0.0–0.4 V. **c** The calculated specific capacitance values with respect to various scan rates. **d** Impedance spectra of α-Mn$_2$O$_3$ measured in the frequency range of 0.1 Hz–100 kHz

In order to further characterize the electrochemical performance of the α-Mn$_2$O$_3$ nanorods, Galvanostatic Charge–Discharge (GCD) response has been measured at different current densities with a potential window of 0.0–0.4 V as shown in Fig. 5b. The GCD curves of α-Mn$_2$O$_3$ nanorods exhibit quasi triangular shaped non-linear asymmetric charge–discharge phenomena at different current densities. The discharge time is long indicating excellent electrochemical performance of α-Mn$_2$O$_3$ nanorods. The quasi-triangular shape of all the charge–discharge curves reveals the occurrence of Faradaic pseudocapacitive reaction in the supercapacitor [29]. Specific capacitance value (C_s) is calculated for various current densities at 1, 2, 3, 4, 5, 10 A g^{-1} and the value are found to be 1180, 1035, 930, 870, 850, 525 F g^{-1} respectively. The corresponding specific capacitance (C_s) values from galvanostatic charge–discharge

studies [30] are calculated using the following formula,

$$C_s = \frac{I\Delta t}{m.\Delta V}, \tag{2}$$

Here I is the current density (Ag^{-1}), C_s is the specific capacitance (Fg^{-1}), Δt is the discharge time (s), ΔV is the discharge potential window (V), and m is the mass of the α-Mn$_2$O$_3$ active electrode material (g). The α-Mn$_2$O$_3$ nanorod electrode exhibits excellent specific capacitance values and the results are comparable and better performance with the reported values of similar compounds. Nelson et al. reported Mn$_2$O$_3$ nanorods synthesized via sonochemical method which yielded specific capacitance of 656 Fg^{-1} at the current density of 1 Ag^{-1} [30]. In another report, You-Hyun et al. reported mesoporous Mn$_2$O$_3$ nanoparticles with specific capacitance of 460 Fg^{-1} at scan rate of 10 mVs^{-1} [15].

Figure 5d shows Nyquist plot of supercapacitor with α-Mn_2O_3nanorod electrode measured in the frequency range of 0.1 Hz–100 kHz. The results of impedance spectra show a 45° slope connected to a slanting spike which represents a Warburg element and capacitance nature of the electrode, respectively. The impedance data is fit with an equivalent circuit which indicates a double layer capacitance (C_{dl}) in parallel with charge transfer resistance (R_{ct}) and a Warburg diffusion (W) element in series with Faradaic pseudo-capacitance (C_{pseudo}) as illustrated in Fig. 5d-inset. In the high frequency region, there is no trace for semicircle whereas only the diffusion element and a linear slope appears which reveals the Faradaic pseudo-capacitance behaviour of the supercapacitor [15].

Figure 6 shows the capacitance retention percentage of supercapacitor withα-Mn_2O_3 nanorods for 1000 charge–discharge cycles at 15 A g^{-1} current density. In the first 200 cycles, the capacitance retention of α-Mn_2O_3 nanorod electrode rapidly fades down to 86% but the later cycles show relatively stable until 1000 cycles. The capacitance retention of α-Mn_2O_3 nanorod at 1000th cycle shows 69% which reveals excellent stability and structural integrity of the electrode.

3.5 Ex-situ analysis of α-Mn_2O_3 nanorods

In order to understand the morphology, structure and impedance variations of α-Mn_2O_3 nanorod active electrode both before and after 1000 cycles, ex-situ

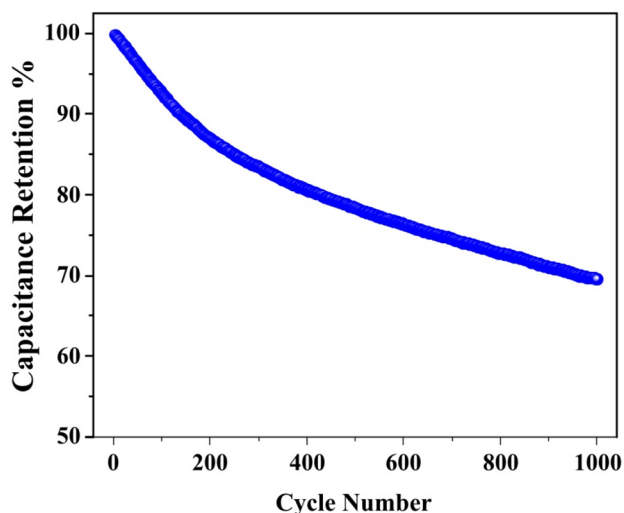investigations have been carried out. Figure 7 shows a comparison of SEM morphology, XRD pattern and impedance spectrum of α-Mn_2O_3 nanorod electrode measured both before and after 1000 cycles of electrochemical measurements. The SEM morphology of as synthesized α-Mn_2O_3 nanorod as shown in Fig. 7a indicates homogeneous morphology along with few bulk agglomerated particles. Figure 7b shows SEM morphology of α-Mn_2O_3 nanorod after 1000 cycles that visualize a thin glassy layer wrapping on the surface of nanorods which might be due to the precipitation of electrolyte. The surface of α-Mn_2O_3 nanorod after cycling shows a smooth morphology and resembles the bare sample without any noticeable cracks or rupture on the surface which reveal morphology retainability.

The XRD pattern shown in Fig. 7c indicates all the relevant peaks (200), (222), (400), (332), (440), (622) corresponding to bare α-Mn_2O_3 appeared in both bare and after cycled samples. The appearance of the XRD peaks corresponding to α-Mn_2O_3 in the sample even after 1000 cycles reveals structural integrity of α-Mn_2O_3. Figure 7d shows impedance spectrum of α-Mn_2O_3 nanorod electrode for both bare and after cycled samples. The α-Mn_2O_3 nanorod samples have very low impedance and no variation in the charge-transfer resistance even after 1000 redox cycles as evidenced from Nyquist plot which reveals the electrode has no internal micro cracks. The ex-situ investigations reveal the α-Mn_2O_3 nanorod electrode has morphology retainability, structural integrity and tensile strength against deterioration.

The nanorod structure plays an important role to maintain structural integrity and good electrochemical performance. The excellent specific capacitance estimated in the α-Mn_2O_3 nanorod electrode might be due to some reasons as follows; (i) The nanorods with large surface area renders more electroactive sites which enhances the specific capacitance; (ii) As evidenced from the ex-situ investigations, the nanorods are uniform and connected to each other in a bound form which is expected to facilitate ionic conductivity of hydroxyl and proton ions; (iii) The nanorods have shorter diffusion path ways that enhances faster ion movement during electrochemical redox reactions; (iv) In addition to nanorods, a small portion of α-Mn_2O_3 nanoparticles present in the matrix of nanorods, and presence of carbon black in the nanorod mixture produces a synergetic effect that enables facile transport of ions during redox reactions which
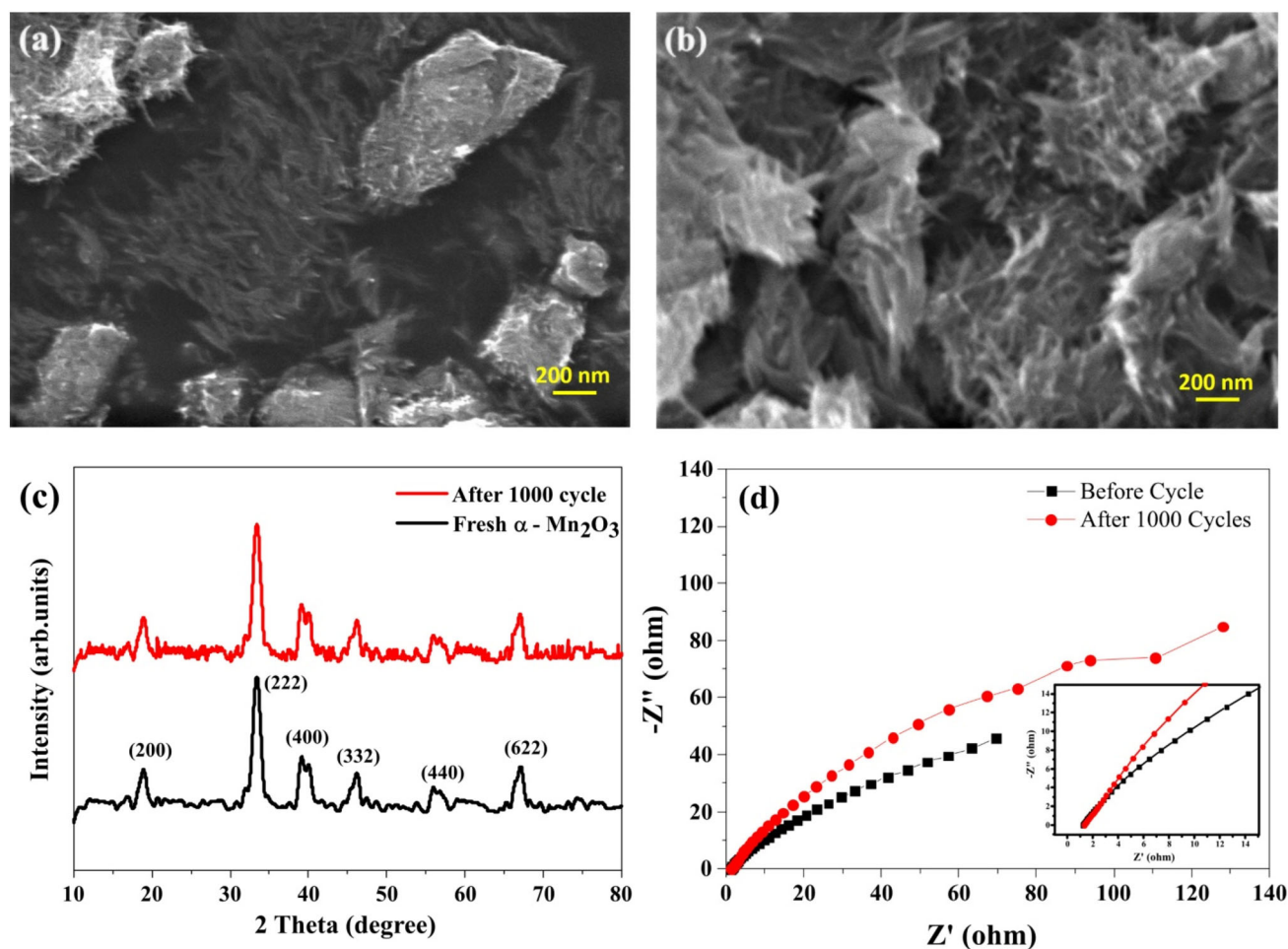
Fig. 6 Capacitance retention percentage of supercapacitor with α-Mn_2O_3 nanorods at 15 A g^{-1} current density

Fig. 7 SEM image of α-Mn$_2$O$_3$ nanorods **a** before and **b** after redox cycling; **c** XRD pattern of α-Mn$_2$O$_3$ nanorods before and after redox cycling; **d** Impedance spectra of supercapacitor with α-Mn$_2$O$_3$ nanorods before and after redox cycling (inset: high frequency range)

enriches the supercapacitive properties of the α-Mn$_2$O$_3$ nanorod electrode.

4 Conclusion

The α-Mn$_2$O$_3$ nanorod electrode has been synthesized by one-pot hydrothermal method for supercapacitor application. XRD analysis of active electrode powder sample confirms cubic phase formation of poly crystalline α-Mn$_2$O$_3$. The SAED pattern indicates (200), (222), (400), and (622) planes correspond to the circular region which reconfirms the polycrystalline nature of α-Mn$_2$O$_3$ as that of XRD pattern. The HR-TEM results reveal the formation of nanorods of α-Mn$_2$O$_3$ with 7 nm diameter and 100 nm average lengths and a high aspect ratio of 1:4. The stoichiometric amount of Mn and oxygen has been confirmed by EDX elemental mapping analysis. The CV results indicate a high specific capacitance of 1377 Fg^{-1} at the scan rate of 5 mV s^{-1}, which might be due to the presence of large active sites and rapid ionic transport in the α-Mn$_2$O$_3$ nanorods. The charge–discharge results depict a typical quasi triangle asymmetric curve corresponds to the Faradaic pseudo-capacitive behavior. The supercapacitor shows good cycling ability and stability with capacity retention of 69% at 1000th cycle. The impedance spectra results reveal the presence of Warburg diffusion element and Faradaic pseudo-capacitance elements in the equivalent circuit fitting. The ex-situ investigations of α-Mn$_2$O$_3$ nanorod electrode reveal uniform morphology, structural integrity, and homogeneous micro structure even after 1000 cycles. The synergetic effect of nanorods with high tensile strength and size effect plays a major role in delivering a good electrochemical performance.

Acknowledgements

Author contributions

All the authors have accepted full responsibility for the content of this manuscript and have given their approval to its submission.

Data availability

The manuscript is associated with all the requested data.

Declarations

Conflict of interest The authors declare that they have no conflict of interest.

References

1. C. Yuan, H. Bin Wu, Y. Xie, X.W.D. Lou, Angew. Chem. Int. Ed. **53**, 1488–1504 (2014). https://doi.org/10.1002/anie.201303971
2. N. Sui, Y. Duan, X. Jiao, D. Chen, J. Phys. Chem. C. **113**, 8560–8565 (2009). https://doi.org/10.1021/jp810452k
3. P. Umek, A. Gloter, M. Pregelj, R. Dominko et al., J. Phys. Chem. C. **113**, 14798–14803 (2009). https://doi.org/10.1021/jp9050319
4. A.L.M. Reddy, M.M. Shaijumon, S.R. Gowda, P.M. Ajayan, J. Phys. Chem. C. **114**, 658–663 (2010). https://doi.org/10.1021/jp908739q
5. S.R.S. Prabaharan, T. Nathan, M. Cloke, J. Nanomater. (2008). https://doi.org/10.1155/2008/948183
6. Z.Y. Yuan, T.Z. Ren, G. Du, B.L. Su, Chem. Phys. Lett. **389**, 83–86 (2004). https://doi.org/10.1016/j.cplett.2004.03.064
7. J. Cao, Y. Zhu, K. Bao, L. Shi et al., J. Phys. Chem. C. **113**, 17755–17760 (2009). https://doi.org/10.1021/jp905482z
8. W.N. Li, L. Zhang, S. Sithambaram, J. Yuan et al., J. Phys. Chem. C. **111**, 14694–14697 (2007). https://doi.org/10.1021/jp0745539
9. M. Liu, G.J. Zhang, Z.R. Shen et al., Solid State Sci. **11**, 118–128 (2009). https://doi.org/10.1016/j.solidstatesciences.2008.05.020
10. Z.Y. Li, M. Shaheer Akhtar, P.T.M. Bui et al., Chem. Eng. J. **330**, 1240–1247 (2017). https://doi.org/10.1016/j.cej.2017.08.060
11. W. Li, J. Shao, Q. Liu et al., Electrochim. Acta. **157**, 108–114 (2015). https://doi.org/10.1016/j.electacta.2015.01.056
12. C. Yuan, L. Hou, L. Yang et al., J. Mater. Chem. **21**, 16035–16041 (2011). https://doi.org/10.1039/c1jm11886b
13. X. Su, X. Yang, L. Yu et al., Cryst. Eng. Comm. **17**, 5970–5977 (2015). https://doi.org/10.1039/c5ce00707k
14. Y. Chen, Y. Zhang, Q.Z. Yao et al., J. Solid State Chem. **180**, 1218–1223 (2007). https://doi.org/10.1016/j.jssc.2007.01.017
15. S. You-Hyun, T.M.B. Phuong, L. Ha-Ryeon, S.A. Mohammad, K.S. Deb, Y. O-Bong, A rapid synthesis of mesoporous Mn_2O_3 nanoparticles for supercapacitor applications. Coatings **9**(631), 1–11 (2019). https://doi.org/10.3390/coatings9100631
16. G. Niu, B. Vilquin, N. Baboux, Microelectron. Eng. **86**, 1700–1702 (2009). https://doi.org/10.1016/j.mee.2009.03.107
17. N.S. Nirmala Jothi, P. Dennis Christy, A.R. Baby Suganthi, G. Ramalingam, P. Sagayaraj, J. Cryst. Growth **316**, 126–131 (2011). https://doi.org/10.1016/j.jcrysgro.2010.12.055
18. B. Deng, H.Y. Huang, Adv. Mater. Res. **1033–1034**, 1040–1043 (2014). https://doi.org/10.4028/www.scientific.net/AMR.1033-1034.1040
19. S.E.H. Murph, C.J. Murphy et al., Cryst. Growth Des. **15**, 1968–1974 (2015). https://doi.org/10.1021/acs.cgd.5b00123
20. N. Krishna Chandar, R. Jayavel, Mater. Res. Bull. **50**, 417–420 (2014). https://doi.org/10.1016/j.materresbull.2013.11.006
21. S. Ravichandran, G. Ramalingam, Synthesis, optical and morphological studies of Sol-Gel derived ZnO/PVP one dimensional nano-composite. J. Nanosci. Nanotechnol. **1**(2), 39–43 (2013)
22. R. Najjar, A.M. Abdel-Gaber, R. Awad, Electrochemical corrosion behaviour of carbon steel in acidic media in presence of Mn_2O_3 nanoparticles synthesized at different pH.

J. Electrochem. Sci. **13**, 8723–8735 (2018). https://doi.org/10.20964/2018.09.50

23. K.S. Avinash, K.D. Tarun, G.B.V.S. Lakshmi, R.S. Pratima, Dimanganese trioxide (Mn_2O_3) based label-free electrochemical biosensor for detection of Aflatoxin-B1. Bioelectrochemistry **137**, 107684 (2021). https://doi.org/10.1016/j.bioelechem.2020.107684

24. M. Pudukudy, Z. Yaakob, Synthesis, characterization, and photocatalytic performance of mesoporous α-Mn_2O_3 microspheres prepared via a precipitation route. J. Nanopart. **2016**, 1–7 (2016). https://doi.org/10.1155/2016/8037013

25. Hu. Lin, Y. Sun, F. Zhang, Q. Chen, Facile synthesis of porous Mn_2O_3 hierarchical microspheres for lithium battery anode with improved lithium storage properties. J. Alloy. Compd. **576**, 86–92 (2013). https://doi.org/10.1016/j.jallcom.2013.04.146

26. D. Garg, M. Kaur, S. Sharma, V. Verma, Effect of CTAB coating on structural, magnetic and peroxidase mimic activity of ferric oxide nanoparticles. Bull. Mater. Sci. **41**(5), 134 (2018). https://doi.org/10.1007/s12034-018-1650-y

27. Yu. Ding, C. Hou, B. Li, Y. Lei, Sensitive hydrazine detection using a porous Mn_2O_3 nanofibersbased sensor. Electroanalysis **23**(5), 1245–1251 (2011). https://doi.org/10.1002/elan.201000660

28. J. Wang, H. Tang, H. Ren et al., Adv. Sci. **1**, 1400011 (2014). https://doi.org/10.1002/advs.201400011

29. N. Kanaujiya, N. Kumar, M. Singh, Y. Sharma, G.D. Varma, J. Energy Storage. **35**, 102302 (2021). https://doi.org/10.1016/j.est.2021.102302

30. A.S. Nelson, M. Mariappan, Rapid and controllable synthesis of Mn2O3 nanorods via a sonochemical method for supercapacitor electrode application. Appl. Phys. A **127**(607), 1–10 (2021). https://doi.org/10.1007/s00339-021-04774-5